Metasurface for multi-channel terahertz beam splitters and polarization rotators

XiaoFei Zang,[1,2] HanHong Gong,[1] Zhen Li,[1] JingYa Xie,[1,2] QingQing Cheng,[1,2] Lin Chen,[1,2] Alexander P. Shkurinov,[3] YiMing Zhu,[1,2,a)] and SongLin Zhuang[1,2]

[1]*Terahertz Technology Innovation Research Institute and Shanghai Key Lab of Modern Optical System, University of Shanghai for Science and Technology, No. 516 JunGong Road, Shanghai 200093, China*
[2]*Terahertz Science Cooperative Innovation Center, Chengdu 610054, China*
[3]*Institute on Laser and Information Technologies of RAS, Branch of the FSRC "Crystallography and Photonics," RAS, Shatura, Moscow Region 140700, Russia*

(Received 9 March 2018; accepted 15 April 2018; published online 26 April 2018)

Terahertz beam splitters and polarization rotators are two typical devices with wide applications ranging from terahertz communication to system integration. However, they are faced with severe challenges in manipulating THz waves in multiple channels, which is desirable for system integration and device miniaturization. Here, we propose a method to design ultra-thin multi-channel THz beam splitters and polarization rotators simultaneously. The reflected beams are divided into four beams with nearly the same density under illumination of linear-polarized THz waves, while the polarization of reflected beams in each channel is modulated with a rotation angle or invariable with respect to the incident THz waves, leading to the multi-channel polarization rotator (multiple polarization rotation in the reflective channels) and beam splitter, respectively. Reflective metasurfaces, created by patterning metal-rods with different orientations on a polyimide film, were fabricated and measured to demonstrate these characteristics. The proposed approach provides an efficient way of controlling polarization of THz waves in various channels, which significantly simplifies THz functional devices and the experimental system. *Published by AIP Publishing.*
https://doi.org/10.1063/1.5028401

Terahertz (THz) science and technology has attracted considerable attention in physics, chemistry, and biology because of its applications in non-destructive imaging, wireless communication, and spectroscopic sensing. For a utility THz system, it is not only determined by the high-efficiency source and detectors but also depends on the high-quality components. However, the lack of high-performance functional devices, such as filters, modulators, beam splitters, and polarization rotators, has restricted the development of practical THz wave systems and applications. THz beam splitters and polarization rotators are two fundamental THz components with wide applications in the coherent THz measurement system and sophisticated organic structure analysis, respectively. Conventionally, metallic wire-grating, pellicle, and silicon-based THz beam splitters are commonly used.[1–3] But they suffer from the oblique illumination and complicated fabrication process due to multiple layers of different materials. Although Faraday effects and chiral materials are proposed to manipulate the optical rotation, they show intrinsic limits in weak magneto-optical effects and weak optical activity in naturally occurring chiral materials.[4,5]

Metasurfaces, the two-dimensional counterparts of metamaterials, have capabilities of manipulating the light's phase, intensity, and polarization, resulting in various functionalities such as generalized Snell's law of refraction,[6,7] metalenses,[8–11] spin-controlled photonics,[12,13] spin-Hall effects,[14–16] vortex beam generation,[17,18] and holograms.[19–24] Benefiting from the ultrathin characteristic, easy fabrication process, and high-efficiency in manipulating the wavefront of THz waves, broadband non-polarizing THz beam splitters that split the incident THz waves into two beams can be realized by designing proper phase gradient with dielectric rods.[25] Metasurfaces can also be applied to design waveplates,[26–30] which mimics the functionality of the birefringent material. For example, a metasurface consisting of a pair of subunits with relative deviation is applied to generate a fixed phase-shift between the left and right circularly polarized components of the incident light, leading to the polarization rotation.[31–33] In addition, transmission-type dielectric metasurfaces have been proposed to modulate beam polarization with high-efficiency.[34,35] However, the above metasurface-based functional devices are limited in unwanted higher diffraction orders, narrow-band performance, and particularly in manipulating the wavefront in the single-channel. Nevertheless, a single device with more functionalities (or polarizations) in multiple channels is a continuing trend for functional devices relating to the system integration and device miniaturization. Inspired by this, we propose a method to design ultra-thin, high-efficiency, and broadband THz beam splitters and polarization rotators. We experimentally demonstrate such ultrathin THz devices that can modulate polarization rotation or keep polarization fixed (without polarization rotation) in multiple channels. The developed devices with controllable generation of arbitrary polarization distributions in multiple channels may be of great importance for future development of advanced multifunctional devices and multichannel information processing.

Figure 1 shows schematic illustrations of the multi-channel THz beam splitter and polarization rotator. A linearly polarized THz beam impinges on the sample, and four beams are reflected into different directions (corresponding

a)Author to whom correspondence should be addressed: ymzhu@usst.edu.cn

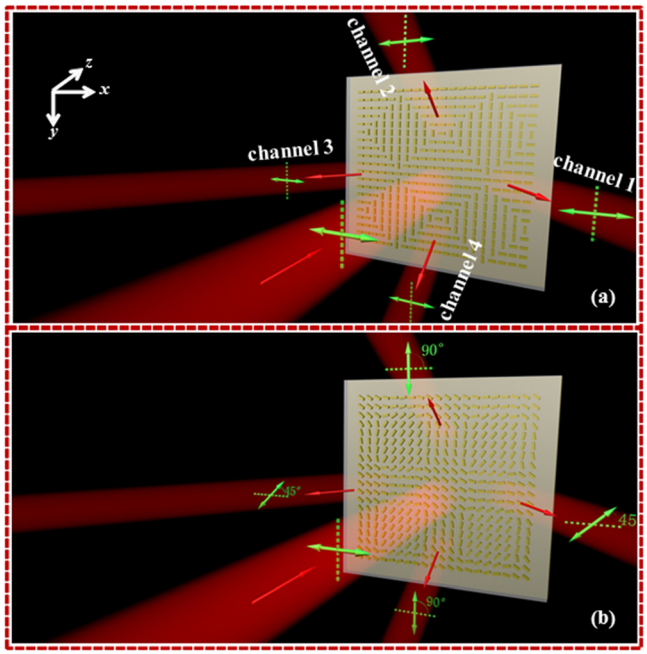

FIG. 1. Schematic of the metasurface-based multi-channel THz beam splitter (a) and polarization rotator (b). The reflected beams are divided into four beams with the corresponding polarization in each channel being the same (a) or rotated with an angle (b) as the incident THz waves.

to four reflective channels). For the THz beam splitter [see Fig. 1(a)], the reflected beams in the four channels have the same polarization with respect to the incident THz wave, which means that all of them are polarized along the x-axis. In contrast, for the polarization rotator [see Fig. 1(b)], each reflected beam is modulated with different polarization rotations, leading to the polarization manipulation in multiple channels. Here, the designed rotation angle in the $\pm x$ axis (channel 1 and channel 3) is 45° while it is 90° in the $\pm y$ axis (channel 2 and channel 4).

The fundamental principle for THz beam splitters and polarization rotators is given as follows. For an incident linearly polarized THz beam, it can be considered as the superposition of two circularly polarized beams with opposite helicity, which can be written as

$$\begin{bmatrix} 1 \\ 0 \end{bmatrix} = \frac{1}{2}\left(\begin{bmatrix} 1 \\ i \end{bmatrix} + \begin{bmatrix} 1 \\ -i \end{bmatrix} \right). \tag{1}$$

When the linearly polarized THz wave interacts with the reflective-type metasurface, it is divided into four beams with the predesigned polarization rotation in each channel. Taking $\pm x$-axis channels (channel 1 and channel 3) for example, the designed polarization rotation angle of the reflective beams is assumed as φ_1 and the corresponding Jones vector is (the detail explanation of polarization rotation of the linear-polarized beam is shown in Ref. 36)

$$\begin{bmatrix} \cos\varphi_1 \\ \sin\varphi_1 \end{bmatrix} = \frac{1}{2}\begin{bmatrix} 1 \\ -i \end{bmatrix} \exp(i\varphi_1) + \frac{1}{2}\begin{bmatrix} 1 \\ i \end{bmatrix} \exp(-i\varphi_1). \tag{2}$$

In order to realize the required functionality, i.e., polarization rotation in multiple channels, the off-axis configuration[37] is adopted to eliminate the effect of the non-converted mode. Here, an additional phase profile that has the capability of generating a pair of centrosymmetrically distributed off-axis beams under the illumination of the linearly polarized beam is needed,[37] and the required Jones vector is given by

$$\begin{aligned} &\frac{1}{2}\left\{ \begin{bmatrix} 1 \\ -i \end{bmatrix} \exp(i\varphi_1) * \exp(i\delta_x) + \begin{bmatrix} 1 \\ i \end{bmatrix} \exp(-i\varphi_1) \right. \\ &\quad \left. * \exp(-i\delta_x) \right\} + \frac{1}{2}\left\{ \begin{bmatrix} 1 \\ -i \end{bmatrix} \exp(i\varphi_1) * \exp(-i\delta_x) \right. \\ &\quad \left. + \begin{bmatrix} 1 \\ i \end{bmatrix} \exp(-i\varphi_1) * \exp(i\delta_x) \right\} \\ &= \begin{bmatrix} \cos\varphi_1 \\ \sin\varphi_1 \end{bmatrix} \exp(i\delta_x) + \begin{bmatrix} \cos\varphi_1 \\ \sin\varphi_1 \end{bmatrix} \exp(-i\delta_x), \end{aligned} \tag{3}$$

where $\pm\delta_x$ is the phase profile, which is utilized to generate a symmetrical dual phase-gradient along the $\pm x$-axis. Here, when phase profile δ_x is introduced, the linear THz waves (with Jones vector of $[\cos\varphi_1 \quad \sin\varphi_1]^T$) are divided into two oblique reflected modes with the corresponding Jones vectors of $[1 \quad i]^T e^{-i\varphi_1}$ (in channel 3) and $[1 \quad -i]^T e^{i\varphi_1}$ (in channel 1), respectively (T represents the matrix transpose). For the phase profile $-\delta_x$, the corresponding linear THz waves can be split into two oblique reflected modes with the Jones vectors of $[1 \quad -i]^T e^{i\varphi_1}$ (in channel 3) and $[1 \quad i]^T e^{-i\varphi_1}$ (in channel 1), respectively. When the dual phase-gradient ($\pm\delta_x$) is applied into the metasurface, the Jones vector in channel 1 (and channel 3) is $[1 \quad -i]^T e^{i\varphi_1} + [1 \quad i]^T e^{i\varphi_1} = [\cos\varphi_1 \quad \sin\varphi_1]^T$, leading to two reflected linear-polarized THz modes (with the desired polarization rotation angle of φ_1) in channel 1 and channel 3.

The required phase distribution for $\pm x$-axis channels is described as

$$\Phi(x) = \arg(\exp[i(\varphi_1 + \delta_x)] + \exp[i(\varphi_1 - \delta_x)]). \tag{4}$$

Accordingly, the total phase distribution for the four channels is governed by

$$\begin{aligned} \Phi(x,y) = \arg\{ &\exp[i(\varphi_1 + \delta_x)] + \exp[i(\varphi_1 - \delta_x)] \\ &+ \exp[i(\varphi_2 + \delta_y)] + \exp[i(\varphi_2 - \delta_y)] \}, \end{aligned} \tag{5}$$

in which φ_2 and $\pm\delta_y$ are the rotating angles and phase-gradient along the $\pm y$-axis, respectively. It should be noted that the device is degraded into four-channels of the beam splitter for $\varphi_1 = \varphi_2 = 0$, where the four reflected beams have the same polarization relative to the incident THz waves. Although the manipulation of polarization demonstrated in this paper is in four channels, this method can be readily extended to control polarization in more channels.

The multi-channel THz beam splitter and polarization rotator can be designed by patterning metal-rods with different orientations on a polyimide film, as shown in Figs. 2(a) and 2(b). The samples are fabricated in the traditional photolithography method. The rotation angle of each metal-rod is exactly determined by Eq. (5). The detailed geometric parameters [see Fig. 2(c)] are selected as follows: $L = 95\ \mu$m (length of the rod), $w = 34\ \mu$m (width of the rod), $p = 120\ \mu$m

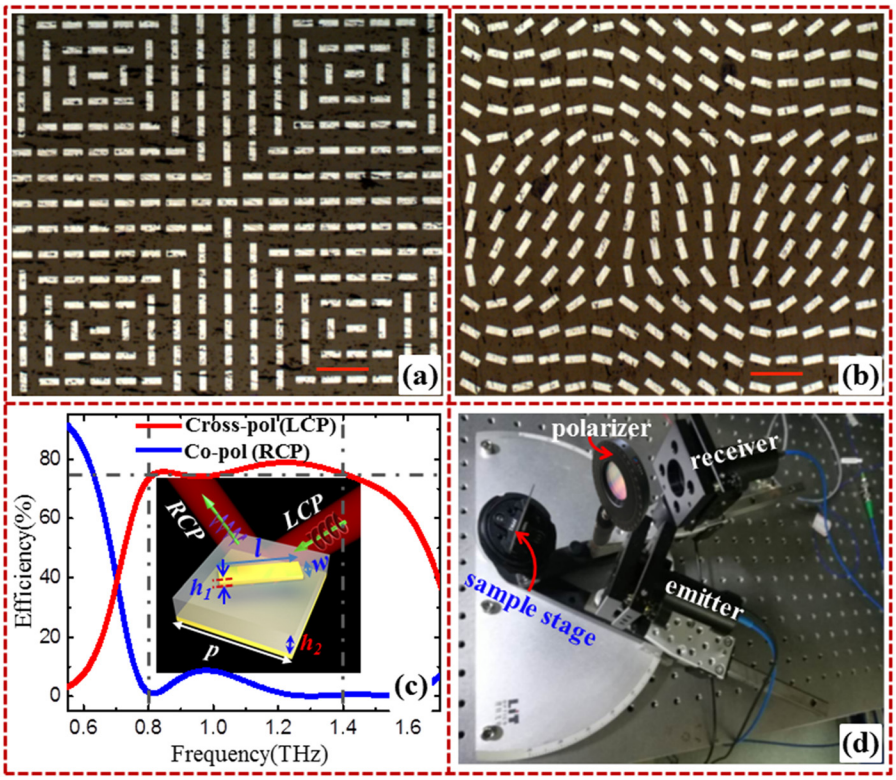

FIG. 2. (a) and (b) The optical images of the fabricated THz beam splitter and polarization rotator, respectively. (c) The simulated cross-polarization (reflected RCP THz waves) and co-polarization (reflected LCP THz waves) efficiency for the unit cell (inset) upon the normal incidence. (d) The experimental set-up. The scale bar in (a) and (b) is 240 μm.

(period), $h_1 = 150$ nm (thickness of the rod and substrate), and $h_2 = 25$ μm [thickness of the spacer (polyimide film)]. The thickness of the sample is 25.3 μm, which is much smaller than $\lambda/10$ [the central wavelength of the sample is about $\lambda = 273$ μm ($f = 1.1$ THz)]. The permittivity of the polyimide is $\varepsilon_{pi} = 3.5 + 0.035i$, and the electrical conductivity of gold is 4.561×10^7 S/m. Figure 2(c) shows the simulated conversion efficiency of a single metal-rod. The conversion efficiency is over 75% in a broadband regime ranging from 0.8 to 1.4 THz. Here, the conversion efficiency is defined as the ratio between the power of the RCP (right-hand circular polarized) reflected THz waves and the incident power [LCP (left-hand circular polarized) incident THz waves]. We experimentally study the properties of the designed devices by using a full-fiber THz time-domain microscopy system [see Fig. 2(d)]. Here, two fiber-based THz photoconductive antennas are mounted on the rotatable stage, in which one is employed as a transmitter and the other is a receiver. The transmitter is excited by 780 nm laser pulses generated from the femtosecond laser. A linearly polarized THz beam is normally incident on the sample (with the transmitter fixing on the platform), and the receiver is rotated on the stage to collect the reflected THz waves. A linear polarizer is located in front of the receiver to detect the polarization direction of the reflective waves by rotating itself.

The simulated and measured results of the normalized I (power distribution relative to angle) for channel 1 are shown in Fig. 3. The rotating angles and phase-gradient of the metal-rods are selected as $\varphi_1 = \varphi_2 = 0$ and $\delta_x = \delta_y = \pi/5$, respectively. The position of the curve (the normalized power distribution) peak denotes the polarization direction of the reflected THz beams. As a proof-of-concept demonstration, we measure the sample in four frequencies, i.e., 0.8, 1.0, 1.2, and 1.4 THz, to verify the properties of the designed device, since the simulated conversion efficiency of the metal-rod is over 75% ranging from 0.8 to 1.4 THz [see Fig. 2(c)]. For the x-polarized incident THz waves, the peaks of the normalized power distribution are located in the $\pm x$-axis, which demonstrates that the polarization state of the reflected THz beam in channel 1 is the same as the incident THz waves. In this case, the polarization states of the reflected waves in other channels are also consistent with the incident THz waves (not shown here). As depicted in Figs. 3(a)–3(d),

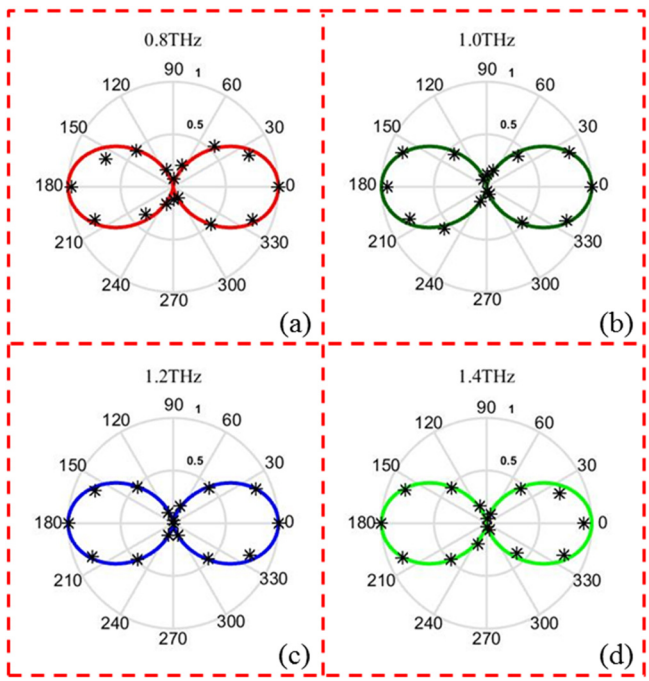

FIG. 3. Simulated (solid curves) and experimentally measured (discrete asterisks) polarization distribution (power distribution along with angle) in channel 1 of the THz beam splitter: (a) $f = 0.8$ THz, (b) $f = 1.0$ THz, (c) $f = 1.2$ THz, and (d) $f = 1.4$ THz. The results are normalized here.

both the simulated and measured results match with each other. The measured angles of the outgoing reflected waves at 0.8, 1.0, 1.2, and 1.4 THz are 18.1°, 14.3°, 12.1°, and 10.1° (for both THz splitters and rotators), respectively, while the calculated reflected angles are 18.21°, 14.48°, 12.02°, and 10.29°, respectively. The measured results agree well with the simulated results. The corresponding conversion efficiency in each channel is shown in Table I. Taking $f = 0.8$ THz for example, the conversion efficiency in the four channels is 16.1%, 16.7%, 15.8%, and 16.5%, respectively, and the total conversion efficiency is 65.1% which is slightly smaller than the calculated case (75%) due to the fabrication error, i.e., the shape deformation of some individual metal-rods. The uniform polarization distribution and nearly identical conversion efficiency in each channel perfectly demonstrate a four-channel of the THz beam splitter here.

Finally, we investigate the THz polarization rotation in multiple channels, since spatial distributions of polarization can be used to record, process, and store information. In this situation, the design parameters of the rotation angles and phase-gradient are as follows: $\varphi_1 = 45°$, $\varphi_2 = 90°$, and $\delta_x = \delta_y = \pi/5$, respectively. According to Eq. (5), the polarization state of the reflected beam in channels 1 and 3 is rotated with a rotation angle of 45° with respect to the incident THz waves while the rotation angle of polarization in channels 2 and 4 is 90°. The corresponding calculated and measured results for channel 1 are shown in Fig. 4. In contrast to THz beam splitters discussed above (without polarization rotation), the peaks in the normalized power distribution are located in the directions of 45° and 225°, respectively. So, the polarization state of the reflected THz beam is rotated anticlockwise with 45° (compared with the incident waves), which means that the metasurface can rotate the x-polarized incident THz beam to the predesigned angle. The experimental results agree well with the numerical simulations, as shown in Figs. 4(a)–4(d). In Figs. 5(a) and 4(d), we also show the corresponding power distribution in channel 2 for $f = 0.8$, 1.0, 1.2, and 1.4 THz, respectively. Now, the peaks in the normalized power distribution are located in the directions of 90° and 270°, respectively, resulting in a 90° of polarization rotation in channel 2. In addition, the polarization rotation angles in channels 3 and 4 are 45° and 90°, respectively (not shown here). Therefore, the designed device has the capability of manipulating polarization states (with different rotation angles) in multiple channels. The conversion efficiency of the multi-channel polarization rotator is shown in Table II. In each measurement frequency point, the total conversion efficiency is more than 57.6%, demonstrating a high-efficiency of the multi-channel polarization rotator.

TABLE I. Conversion efficiency for the THz beam splitter.

	Conversion efficiency			
Channel	0.8 THz	1.0 THz	1.2 THz	1.4 THz
Channel 1	16.1%	16.1%	15.4%	15.6%
Channel 2	16.7%	16.4%	15.2%	15.3%
Channel 3	15.8%	16.0%	15.5%	16.2%
Channel 4	16.5%	16.8%	16.1%	16.2%

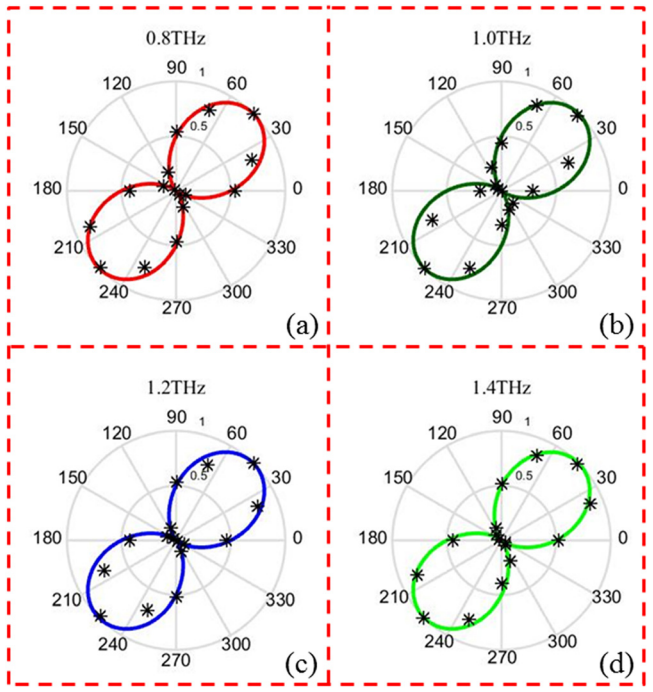

FIG. 4. Simulated (solid curves) and experimentally measured (discrete asterisks) polarization distribution (power distribution along with angle) in channel 1 of the THz polarization rotator: (a) $f = 0.8$ THz, (b) $f = 1.0$ THz, (c) $f = 1.2$ THz, and (d) $f = 1.4$ THz. The results are normalized here.

In summary, we have proposed a method to design the multi-channel metasurface for the control of THz beam splitting and polarization rotation. The multi-channel THz beam splitter and polarization rotator were experimentally demonstrated based on reflective metasurfaces. The polarization states of reflected beams in the four channels can be well modulated with different rotation angles or invariable

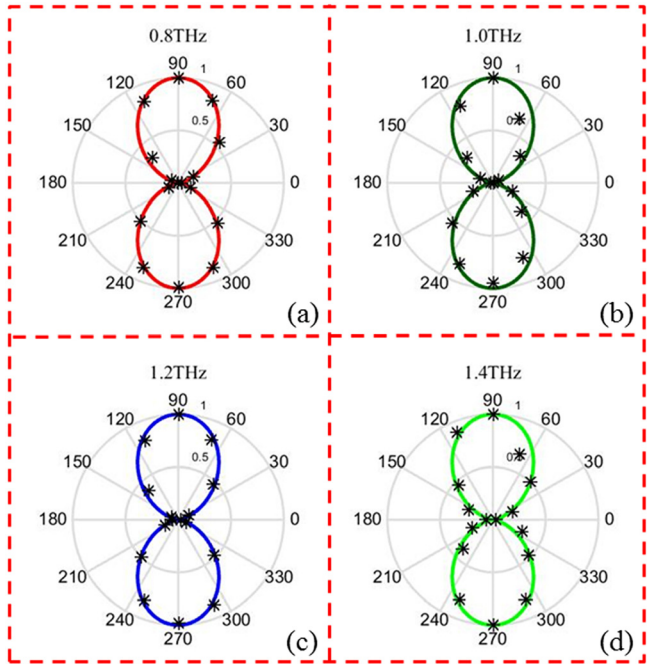

FIG. 5. Simulated (solid curves) and experimentally measured (discrete asterisks) polarization distribution (power distribution along with angle) in channel 2 of the THz polarization rotator: (a) $f = 0.8$ THz, (b) $f = 1.0$ THz, (c) $f = 1.2$ THz, and (d) $f = 1.4$ THz. The results are normalized here.

TABLE II. Conversion efficiency for the THz rotator.

	Conversion efficiency			
Channel	0.8 THz	1.0 THz	1.2 THz	1.4 THz
Channel 1	14.0%	14.5%	14.6%	15.6%
Channel 2	14.7%	14.1%	15.3%	15.5%
Channel 3	14.1%	15.0%	14.6%	15.6%
Channel 4	14.8%	14.5%	15.2%	15.3%

relative to the incident THz waves. The compact multi-channel THz functional devices demonstrated here not only provide a tool to modify the polarization in multiple channels but also open an avenue for device miniaturization and system integration.

This work was supported in part by the National Program on Key Basic Research Project of China (973 Program) (2014CB339806), the Major National Development Project of Scientific Instrument and Equipment (2017YFF0106300, 2016YFF0100503), Natural Science Foundation of Shanghai (18ZR1425600), State Key Laboratory of Advanced Optical Communication Systems and Networks, Shanghai Jiao Tong University, China (2018GZKF03004), National Natural Science Foundation of China (61307126, 61722111), the Key Scientific and Technological Project of Science and Technology Commission of Shanghai Municipality (15DZ0500102), Shanghai leading talent (2016-019), Young Yangtse Rive Scholar (Q2016212), and Shanghai international joint laboratory project (17590750300).

[1]C. W. Berry, J. Moore, and M. Jarrahi, Opt. Express **19**, 1236 (2011).
[2]C. W. Berry and M. Jarrahi, J. Infrared, Millimeter, Terahertz Waves **33**, 127 (2012).
[3]A. Rizea, Opto-Electron. Rev. **20**, 96 (2012).
[4]D. Floess, J. Y. Chin, A. Kawatani, D. Dregely, H. U. Habermeier, T. Weiss, and H. Giessen, Light: Sci. Appl. **4**, e284 (2015).
[5]J. Y. Chin, T. Steinle, T. Wehlus, D. Dregely, T. Weiss, V. I. Belotelov, B. Stritzker, and H. Giessen, Nat. Commun. **4**, 1599 (2013).
[6]N. F. Yu, P. Genevet, M. A. Kats, F. Aieta, J. P. Tetienne, F. Capasso, and Z. Gaburro, Science **334**, 333 (2011).
[7]L. Huang, X. Chen, H. Mühlenbernd, G. Li, B. Bai, Q. Tan, G. Jin, T. Zentgraf, and S. Zhang, Nano Lett. **12**, 5750 (2012).
[8]X. Chen, L. Huang, H. Mühlenbernd, G. Li, B. Bai, Q. Tan, G. Jin, C. Qiu, S. Zhang, and T. Zentgraf, Nat. Commun. **3**, 1198 (2012).
[9]X. Chen, Y. Zhang, L. Huang, and S. Zhang, Adv. Opt. Mater. **2**, 978 (2014).
[10]M. Khorasaninejad, Z. Shi, W. Chen, V. Sanjeev, A. Zaidi, and F. Capasso, Nano Lett. **17**, 1819 (2017).
[11]S. M. Wang, P. C. Wu, V.-C. Su, Y.-C. Lai, C. H. Chu, J.-W. Chen, S.-H. Lu, J. Chen, B. B. Xu, C.-H. Kuan, T. Li, S. N. Zhu, and D. P. Tsai, Nat. Commun. **8**, 187 (2017).
[12]N. Shitrit, I. Yulevich, E. Maguid, D. Ozeri, D. Veksler, V. Kleiner, and E. Hasman, Science **340**, 724 (2013).
[13]L. L. Huang, X. Z. Chen, B. F. Bai, Q. Tan, G. F. Jin, T. Zentgraf, and S. Zhang, Light: Sci. Appl. **2**, e70 (2013).
[14]X. Yin, Z. Ye, J. Rho, Y. Wang, and X. Zhang, Science **339**, 1405 (2013).
[15]X. Lin, X. Zhou, X. Yi, W. Shu, Y. Liu, S. Chen, H. Luo, S. Wen, and D. Fan, Light: Sci. Appl. **4**, e290 (2015).
[16]W. Luo, S. Xiao, Q. He, S. Sun, and L. Zhou, Adv. Opt. Mater. **3**, 1102 (2015).
[17]M. Q. Mehmood, S. Mei, S. Hussain, K. Huang, S. Y. Siew, L. Zhang, T. Zhang, X. Ling, H. Liu, J. Teng, A. Danner, S. Zhang, and C. Qiu, Adv. Mater. **28**, 2533 (2016).
[18]F. Yue, D. Wen, C. Zhang, B. D. Gerardot, W. Wang, S. Zhang, and X. Chen, Adv. Mater. **29**, 1603838 (2017).
[19]X. J. Ni, A. V. Kildishev, and V. M. Shalaev, Nat. Commun. **4**, 2807 (2013).
[20]G. X. Zheng, H. Muhlenbernd, M. Kenney, G. X. Li, T. Zentgraf, and S. Zhang, Nat. Nanotechnol. **10**, 308 (2015).
[21]D. D. Wen, F. Y. Yue, G. X. Li, G. X. Zheng, K. Chan, S. M. Chen, M. Chen, K. F. Li, P. Wing, H. Wong, K. W. Cheah, E. Y. B. Pun, S. Zhang, and X. Z. Chen, Nat. Commun. **6**, 8241 (2015).
[22]H. W. Huang, W. T. Chen, W. Y. Tsai, P. C. Wu, C. M. Wang, G. Sun, and D. P. Tsai, Nano Lett. **15**, 3122–3127 (2015).
[23]B. Wang, F. L. Dong, Q. T. Li, D. Yang, C. W. Sun, J. J. Chen, Z. W. Song, L. H. Xu, W. G. Chu, Y. F. Xiao, Q. H. Gong, and Y. Li, Nano Lett. **16**, 5235 (2016).
[24]X. Li, L. Chen, Y. Li, X. Zhang, M. Pu, Z. Zhao, X. Ma, Y. Wang, M. Hong, and X. Luo, Sci. Adv. **2**, e1601102 (2016).
[25]M. Wei, Q. Xu, Q. Wang, X. Zhang, Y. Li, J. Gu, Z. Tian, X. Zhang, J. Han, and W. Zhang, Appl. Phys. Lett. **111**, 071101 (2017).
[26]N. Yu, F. Aieta, P. Genevet, M. A. Kats, Z. Gaburro, and F. Capasso, Nano Lett. **12**, 6328 (2012).
[27]N. Grady, J. Heyes, D. Chowdhury, Y. Zeng, M. Reiten, A. Azad, A. Taylor, D. Dalvit, and H. Chen, Science **340**, 1304 (2013).
[28]B. Yang, W. M. Ye, X. D. Yuan, Z. H. Zhu, and C. Zeng, Opt. Lett. **38**, 679 (2013).
[29]R. Fan, Y. Zhou, X. Ren, R. Peng, S. Jiang, D. Xu, X. Xiong, X. Huang, and M. Wang, Adv. Mater. **27**, 1201 (2015).
[30]S. Jiang, Phys. Rev. X **4**, 021026 (2014).
[31]A. Shaltout, J. Liu, V. M. Shalaev, and A. V. Kildishev, Nano Lett. **14**, 4426 (2014).
[32]P. C. Wu, W. Y. Tsai, W. T. Chen, Y. W. Huang, T. Y. Chen, J. W. Chen, C. Y. Liao, C. H. Chu, G. Sun, and D. P. Tsai, Nano Lett. **17**, 445 (2017).
[33]D. Wen, F. Yue, C. Zhang, X. Zang, H. Liu, W. Wang, and X. Chen, Appl. Phys. Lett. **111**, 023102 (2017).
[34]D. Lin, P. Fan, E. Hasman, and M. L. Brongersma, Science **345**, 298 (2014).
[35]A. Arbabi, Y. Horie, M. Bagheri, and A. Faraon, Nat. Nanotechnol. **10**, 937 (2015).
[36]X. Zang, F. Dong, F. Yue, C. Zhang, L. Xu, Z. Song, M. Chen, P. Chen, G. S. Buller, Y. Zhu, S. Zhuang, W. Chu, S. Zhang, and X. Chen, Adv. Mater. **30**, 1707499 (2018).
[37]F. Yue, C. Zhang, X. Zang, D. Wen, B. D. Gerardot, S. Zhang, and X. Chen, Light: Sci. Appl. **7**, 17129 (2018).